

Land-cover Classification Using Radarsat and Landsat Imagery for St. Louis, Missouri

Heng Huang, Justin Legarsky, and Maslina Othman

Abstract

This paper presents the potential of integrating radar data features with optical data to improve automatic land-cover mapping. For our study area of St. Louis, Missouri, Landsat ETM+ and Radarsat images are orthorectified and co-registered to each other. A maximum likelihood classifier is utilized to determine different land-cover categories. Ground reference data from sites throughout the study area are collected for training and validation. The variations in classification accuracy due to a number of radar imaging processing techniques are studied. The relationship between the processing window and the land classification is also investigated. In addition, the Landsat images are fused with several combinations of processed radar features. The classification accuracies from the Landsat and radar feature combinations are studied. Our research finds that fusion of multi-sensor data improves the classification accuracy over a single Landsat sensor, although different processing techniques on radar images are required to obtain the best results. In our study, fusion of Landsat images and Radarsat feature combinations from a 13×13 entropy window, 9×9 data range widow, and 19×19 mean filter window achieves the highest overall accuracy improvement (10 percent) over the Landsat images alone.

Introduction

As urbanization increases, the infrastructure of cities and municipalities expand simultaneously to meet people's needs and interests. The up-to-date information on geographic issues such as population locations, forests, crops, and water facilities play an important role in scientific analysis and decision-making activities. Satellite remote sensing provides a cost-effective method to obtain current and reliable Earth surface information because of its widespread availability and frequency of update (Donnay *et al.*, 2001).

Optical sensors such as Landsat TM/ETM+ and SPOT have proven an efficient tool for various applications like land-cover mapping (Gong and Howarth, 1990; Ji, 2000), change detection (Green *et al.*, 1994; Singh, 1989), and disaster control (Tapley *et al.*, 2001). These passive optical sensors only receive emissions and reflectance from the scene under

observation. They have limitations in acquiring cloud-free imagery on a regular basis and difficulties in performing spectral classification for certain types of land features (Ulaby *et al.*, 1982).

Compared to optical sensors, active microwave sensors can provide their own illumination of a scene under observation. The longer wavelengths enable penetration of atmospheric conditions such as rain, sleet, fog, haze, smoke, precipitation, and clouds (Haack *et al.*, 2000). Hence, an advantage of active microwave sensors such as Synthetic-Aperture Radar (SAR) is their ability to obtain images under various weather conditions during both day and night (Curlander and McDonough, 1991; Goetz *et al.*, 2000). Due largely to the wavelength, radar and optical sensors have different reflectance interactions with the Earth surface as well. Therefore, radar sensors have the potential to provide additional information that may be combined with optical sensor data for improving land classification (Won *et al.*, 1999).

Recent studies (Haack and Slonecker, 1994; Solberg *et al.*, 1994; Weydahl *et al.*, 1995) utilizing SAR and optical sensor data demonstrated distinct improvements in classification accuracies in contrast to an optical sensor alone. The unprocessed radar images are often complicated by the presence of speckle noise resulting from the constructive and deconstructive interference of reflected signals (Dobson *et al.*, 1992; Richards, 1990). Additional signal processing, such as speckle filtering and texture extraction, may help the interpretation of radar images. For instance, Haack *et al.* (2000) applied the variance texture extraction on Radarsat image to achieve about 10 percent classification accuracy improvement when fused with Landsat images for a study site in Dadaad, Kenya. However, no ascertained filtering or texture technique has been claimed to be the most efficient for all image scenes and classification types.

This research assesses the land-cover classification of St. Louis, Missouri using multi-source imagery. Radar imagery is processed by a number of filtering and texture techniques. The classification accuracies when using each of the techniques are analyzed for the study area. Also, Landsat images are merged with one or multiple Radarsat features to further increase the classification accuracy.

Study Area

This analysis is limited to an area covering St. Louis County, part of St. Charles County, Missouri and part of the State of Illinois. Figure 1 shows the location of this area. Specifically,

Heng Huang is with NextG Networks, Inc., 2216 O'Toole Avenue, San Jose, CA 95131 and was formerly with the Electrical and Computer Engineering Department, University of Missouri-Columbia, MO (hhuang@nextgnetwork.net).

Justin Legarsky and Maslina Othman are with the Electrical and Computer Engineering Department, University of Missouri-Columbia, 349 Engineering Building West, Columbia, MO 65221.

Photogrammetric Engineering & Remote Sensing
Vol. 73, No. 1, January 2007, pp. 037-043.

0099-1112/07/7301-0037/\$3.00/0
© 2007 American Society for Photogrammetry
and Remote Sensing

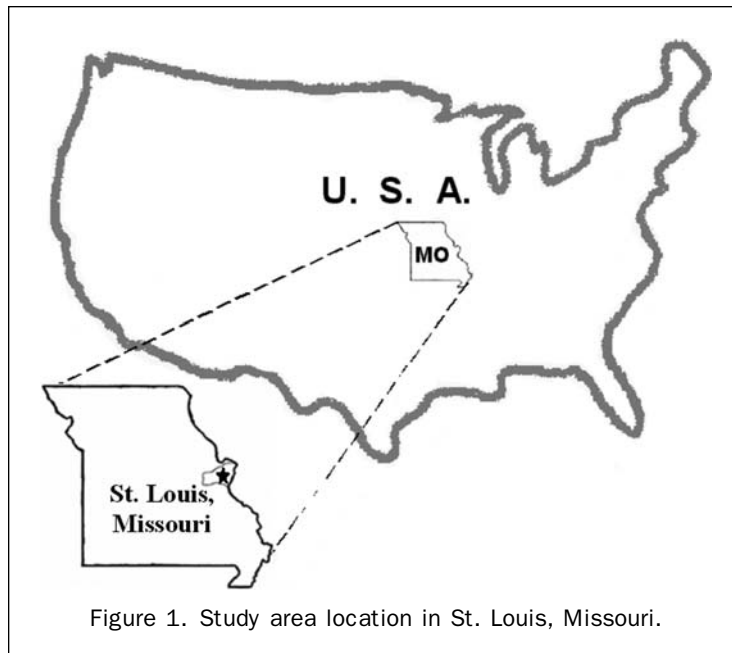


Figure 1. Study area location in St. Louis, Missouri.

this study area is geographically located at the mid-east portion of Missouri in between $38^{\circ}22'51.84''$ and $38^{\circ}54'9.98''$ latitude north, and in between $90^{\circ}7'56.78''$ and $90^{\circ}43'25.71''$ longitude west, which is approximately 53 km by 56 km. Our study area hosts more than one million population and covers the greater St. Louis region.

Satellite Images

Three primary data sets of St. Louis area are obtained for this analysis. The first data set is Canadian Space Agency's (CSA) Radarsat SAR imagery acquired on 12 November 2001. Radarsat's SAR collected the radio intensity data in C-band (5.6 cm) standard beam mode with 12.5 m pixel spacing, which we re-sampled to a 30 m pixel spacing to have a one to one pixel correspondence with the Landsat imagery. Figure 2 shows the radar scene of the study area. St. Louis metropolitan area stretches from the center toward east in this study site. The Missouri River and Mississippi River merge together at the northeastern portion of the scene. The other two data sets are standard Landsat-7 ETM+ imagery, which were acquired on 02 February and 14 June 2002, respectively. The Landsat-7 ETM+ sensor collects data in six visible or infrared bands. We used 30 m pixel spacing for the Landsat imagery. This study examines Landsat-7 ETM+ bands 3, 4, and 5. While we can recommend future investigations using all six bands, the three Landsat bands used in this study (visible red, near infrared, mid infrared) have been shown to provide good analysis results in many land-cover investigations (Haack *et al.*, 2000).

Reference Data

The ground reference data are obtained from high-resolution Ikonos imagery (acquired on 08 April 2001) and Digital Orthophoto Quarter Quadrangles (DOQQs). Orthophotos combine the image characteristics of aerial photographs (collected between 15 June and 16 August 2003) with the geometric qualities of a map. Unlike a standard aerial photograph, relief displacement in DOQQs is removed so that ground features are displayed in their true ground position, which allows for the direct measurement of distance, areas, and positions. The visual interpretation approach is adopted

in this study. Land features with geolocation are examined carefully and registered to the fused optical/radar data set. Multi-source imagery is also examined for crosscheck to reference sources, because reference sources were not collected at same dates as multi-source imagery.

In this research, our study area is classified into seven land-cover categories: forest, water, open, low-density buildings (LDB), median-density buildings (MDB), high-density buildings (HDB), and transportation. Forest includes areas of forest with at least 70 percent crown closure which is found in both urban and rural areas. Water consists of lakes, large rivers, and canals. Open includes agricultural land, rangeland, grassland, golf courses, and major parks where significant; forested areas are not present, but some level of vegetation exists. LDB are mainly residential with homes on large lots, where 10 percent to 30 percent of the region is covered by built-up. MDB are mainly residential with homes on medium or small lots, where 30 percent to 50 percent of the region is covered by built-up. HDB are residential and commercial areas, including row houses, apartments, and/or homes on small lots, where 50 percent to 70 percent of the region is covered by built-up. It also includes the central business districts within major metropolitan areas, primarily consisting of tall buildings. Transportation includes airports, highways, and major roads.

The ground reference data for each land-cover type are collected in a simple random sampling pattern (Campbell, 1996). The randomness of sample locations ensures that all portions of the study area are equally subject to selection for samples, thereby yielding data that accurately represent the area examined. At each random sample location, polygons are selected from each present land-cover type for use as reference data. We selected a large number of random sample locations for sufficient randomness of the reference data throughout the image. The percentage of crown closure and buildings are measured manually by visual interpretation. About half of the reference points are used for training, while the remaining data are used for validation. The locations of training data are separate from the validation data. Table 1 lists the number of pixels and polygons used for each land-cover class. A total of 18,852 pixels are used overall in this study, among which 9,698 pixels are used as training data, while the remaining 9,154 pixels are used to

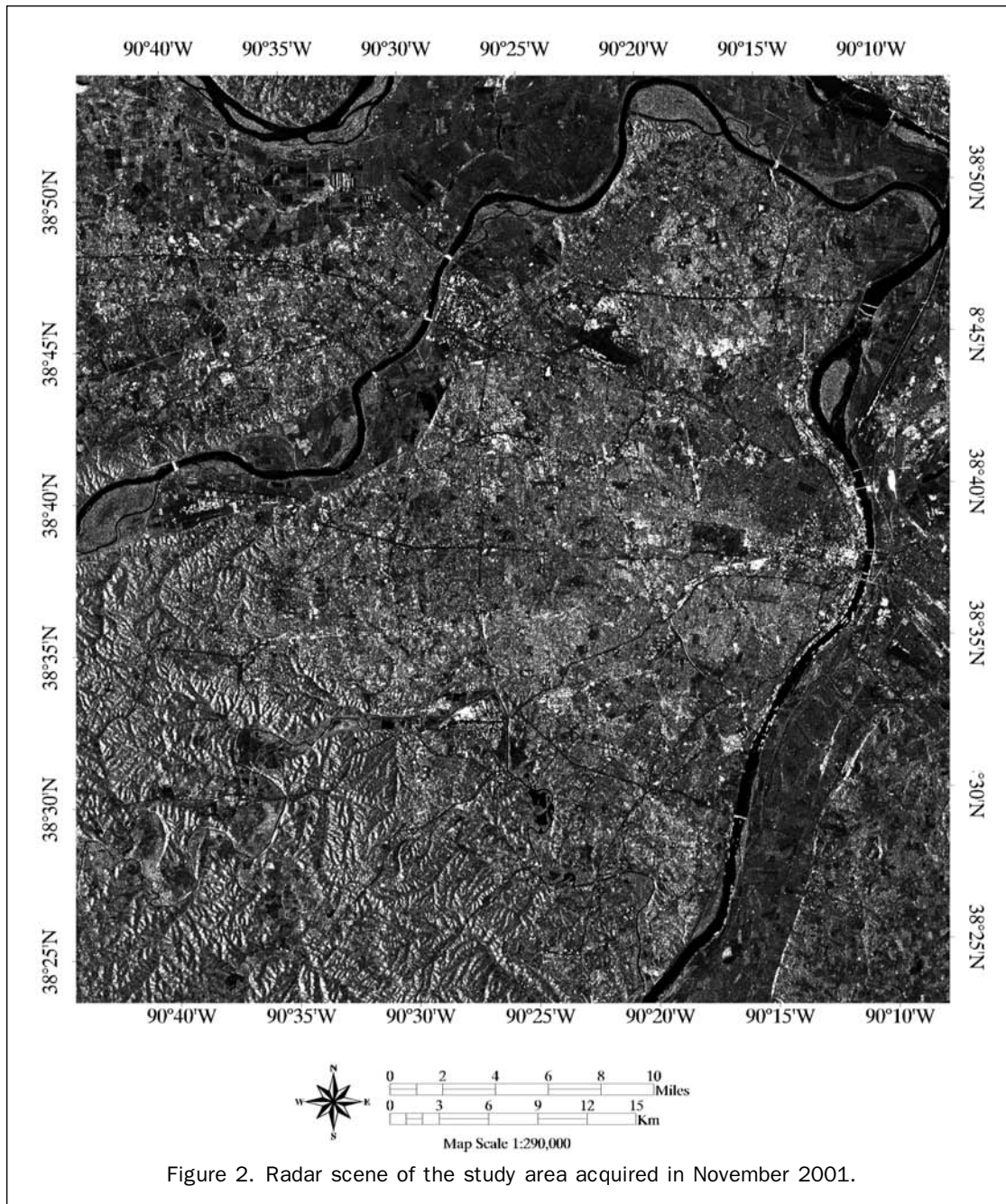


Figure 2. Radar scene of the study area acquired in November 2001.

validate the classification results. Each class has about 2,500 reference data points, which is about one-seventh of the total number.

Methodology

In our study, we digitally classified spatially co-registered radar and optical images, all sampled to the same pixel size. A block diagram of the processing steps is presented in Figure 3. Each block is described in detail below.

Orthorectification

Radarsat imagery and Landsat imagery are orthorectified to the same Universal Transverse Mercator (UTM) map projection by using USGS Spatial Data Transfer Standard (SDTS) Digital Elevation Model (DEM) data with 30 m pixel spacing.

Radarsat data are re-sampled to the 30 m pixel size using the nearest neighbor method, and co-registered pixel by pixel with 30 m pixel size Landsat imagery. For this study, software tools obtained from Alaska Satellite Facility (ASF) are used to orthorectify the Radarsat data, while the Landsat images are orthorectified with commercial PCI software using the satellite orbital model. Readily observable land features (i.e., bridges and highway intersections) are manually examined in the co-registered satellite imagery. We found the spatial misalignment between different images to be typically less than two pixels.

SAR Image Processing

Digital filtering and texture techniques are important tools in image processing and interpretation. Since the presence of speckle noise can result in a high degree of misclassification,

TABLE 1. REFERENCE PIXELS QUANTITY FOR EACH LAND-COVER

| | Forest | | Water | | Open | | LDB | | MDB | | HDB | | Transpiration | | Total | |
|------------|--------|---------|-------|---------|-------|---------|-------|---------|-------|---------|-------|---------|---------------|---------|-------|---------|
| | Pixel | Polygon | Pixel | Polygon | Pixel | Polygon | Pixel | Polygon | Pixel | Polygon | Pixel | Polygon | Pixel | Polygon | Pixel | Polygon |
| Training | 1303 | 28 | 1302 | 30 | 1508 | 27 | 1423 | 17 | 1427 | 20 | 1472 | 15 | 1263 | 16 | 9698 | 153 |
| Validation | 1361 | 29 | 1299 | 29 | 1360 | 21 | 1336 | 22 | 1308 | 26 | 1264 | 20 | 1226 | 15 | 9154 | 162 |
| Total | 2664 | 57 | 2601 | 59 | 2868 | 48 | 2759 | 39 | 2735 | 46 | 2736 | 35 | 2489 | 31 | 18852 | 315 |

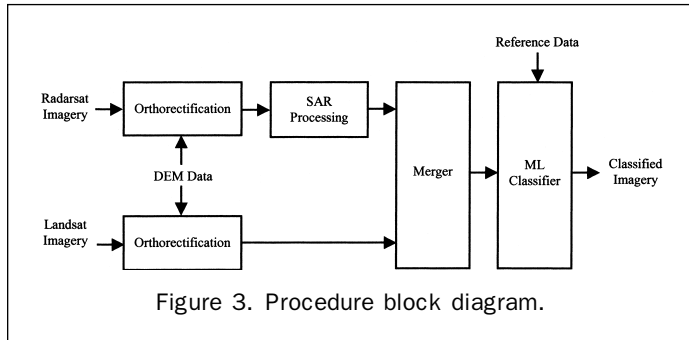


Figure 3. Procedure block diagram.

speckle reduction techniques such as averaging (e.g., mean, LPF, and median) are often used to preprocess raw SAR imagery (Hagg and Sties, 1994). Also, texture features and image metrics may be extracted from radar imagery through various processing techniques to assist SAR image interpretation (Solberg and Anil, 1997). In this research, eight image processing techniques (Gaussian high pass filter (HPF), Gaussian low pass filter (LPF), Laplacian, mean, median, entropy and data range (DR), and variance) are applied to the Radarsat data. These neighborhood (i.e., window) techniques are well described in the literature (Gonzalez, 1987; Russ, 1992; Ludeman, 1986; Proakis *et al.*, 1986; Haralick, 1973). Table 2 lists the brief equation for each processing method applied to Radarsat data in this investigation. $N(z_i)$ is number of pixels having same gray level of z_i in the window. M is total number of pixels in a window. L is the number of gray levels in the window. The variable, μ , is the mean. Variables, x and y , are spatial directions.

In addition, we examined the effects of window size for these processing techniques. Radarsat data are pre-processed using each of the mentioned techniques with window sizes ranging from 3×3 pixels up to 25×25 pixels. The processed radar images are added as additional bands with the Landsat imagery for classification.

Merger

The Landsat-7 ETM+ bands 3, 4, 5 and Radarsat data are merged together into a common image file format, with Radarsat data inserted as extra band(s). This step prepares the fused multi-sensor data for classifications.

Classification

A supervised maximum likelihood (ML) classifier is applied to the fused Landsat/Radarsat data, to perform the land-cover classification in this study. The ML decision rule, implemented quantitatively to consider several classes and several spectral channels simultaneously, assigns a land-cover class to each pixel location of interest that is based on the similarity between the optical spectrum and the radio intensity of different land features. This study uses the ML classifier because it is well utilized in many of the current related research literature (Benediktsson *et al.*, 1999; Kurosu *et al.*, 1999; Strozz *et al.*, 2000). The ML classifier is optimal in the

TABLE 2. SIMPLIFIED EQUATIONS FOR IMAGE PROCESSING

| Processing Name | Brief Summary Formula |
|-----------------|---|
| Gaussian HPF | $1 - \frac{1}{2\pi\delta^2} e^{-\frac{x^2+y^2}{2\delta^2}}$ |
| Gaussian LPF | $\frac{1}{2\pi\delta^2} e^{-\frac{x^2+y^2}{2\delta^2}}$ |
| Laplacian | $\frac{\partial^2 f}{\partial x^2} + \frac{\partial^2 f}{\partial y^2}$ |
| Mean | $\sum_{i=0}^M \frac{N(z_i)}{M}$ |
| Median | Median of the gray levels in the window |
| Entropy | $-\sum_{i=0}^{L-1} \frac{N(z_i)}{M} \ln \frac{N(z_i)}{M}$ |
| Data Range | DR = max - min |
| Variance | $\sum_{i=0}^{L-1} (z_i - \mu)^2 \frac{N(z_i)}{M}$ |

*De-speckling by averaging can be obtained from the mean, LPF, and median processing.

case of equally distributed (e.g., Gaussian distribution) image metrics and texture features (Paola and Schowengerdt, 1995).

This study analyzes three data combinations: (a) Radarsat, November 2001 and Landsat, February 2002; (b) Radarsat, November 2001 and Landsat, June 2002; and (c) Radarsat, November 2001 and Landsat, February and June 2002. Eight processing techniques with various processing window sizes are studied for each data combination. In addition, the best three radar processing metrics are combined to further enhance the classification accuracy.

Results and Discussion

We made a number of observations throughout the course of this investigation. The fusion of Landsat and raw Radarsat images shows additional improvement in overall classification accuracy (about 1 percent increase). Our study shows the dual-season Landsat classification produces higher overall accuracy (about 7 percent) over single-season Landsat classification. We found more than a 7 percent increase in classification accuracy when entropy-processed radar data is merged with the Landsat images. Furthermore, we found more than 10 percent increase in classification accuracy when the best three radar metric images are merged with the Landsat images. The following paragraphs discuss the details of these observations and others.

We found the fusion of entropy-processed Radarsat data alone with Landsat data consistently produced higher classification accuracy than using the other seven preprocessing techniques. We found the 13×13 window size to produce the highest accuracy for the entropy filter. Some filtering techniques (i.e., mean filter) may increase the radiometric resolution, which is defined by the signal variance. Meanwhile, the spatial resolution may decrease (e.g., blurring edges within the image). Texture techniques extract texture information, such as entropy, variance, and data range, from the radar image, which can assist in the image interpretation.

Figure 4 presents the overall validation accuracies for two Landsat data sets and a Radarsat image processed by each of eight techniques with various window sizes. Land classification accuracies from the optical data set (74.44 percent) may provide a baseline for comparison to the fused optical and radar data sets. All the processing techniques at window size 1×1 are equivalent to unprocessed radar data. HPF and Laplacian filter didn't improve the overall accuracy, which trends downward with window size perhaps due to the reduction in low frequency information. The other processing techniques improve the classification, among which entropy filtering resulted in the highest accuracy. Entropy, mean, and data range processing show a clear accuracy peak for a specific window size. The accuracy trend with window size increases for LPF, variance, and median processing to near a saturating value, which is lower than the methods with value peaks and may possibly further decrease with larger window sizes. The overall classification accuracy achieves the peak of 81.04 percent at the entropy window size 13×13 . The other two data combinations produce similar patterns.

Table 3 presents the classification results for different combinations of sensor data. Integrating multi-season Landsat data generates higher accuracies (about 7.5 percent increase), likely due to seasonal land variations, which offer the potential for additional useful information in the classification process. Raw Radarsat data didn't significantly contribute to the overall classification for all three dataset combinations. Individual classes like open, MDB, and transportation have been improved with unprocessed Radarsat data. The accuracy for LDB and HDB decrease after adding the unprocessed radar data. Fusing Landsat data with entropy-filtered Radarsat data consistently improved the overall accuracy by more than 6 percent for all three multi-source combinations. Water and forest have high accuracies in the Landsat only processing. The other class accuracies (i.e., open, LDB, MDB, HDB, and transport) are much lower in the Landsat only processing. The individual classification improvements occur mainly in the classes with the lower accuracy Landsat only processing.

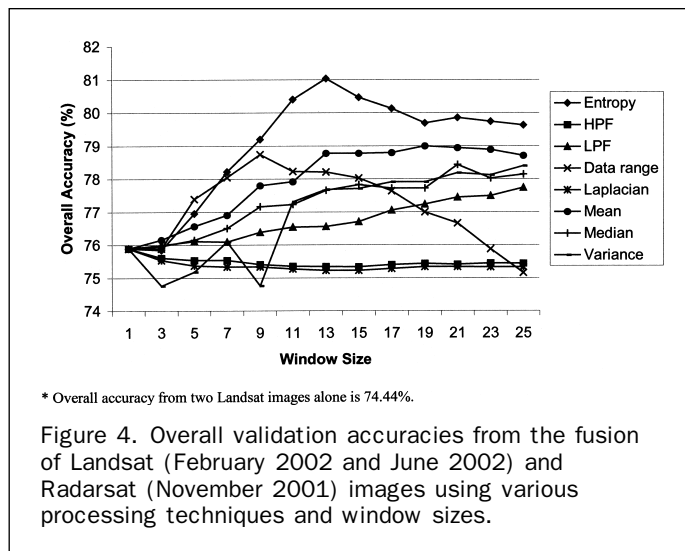


Figure 4. Overall validation accuracies from the fusion of Landsat (February 2002 and June 2002) and Radarsat (November 2001) images using various processing techniques and window sizes.

Especially for MDB and HDB classes (i.e., lowest accuracies in Landsat only processing), the entropy-filtered radar data improved the classification, although the unprocessed radar data only had a small effect on the accuracy. Perhaps, entropy processing of the radar data produces the higher accuracies in the MDB and HDB classes do in part to less class homogeneity and more class texture.

Spectral signatures of all the classes are also extracted from the reference data, which is presented in Table 4. The mean (μ) and standard deviation (δ) of the pixel values were calculated from the training reference points for each land class. Landsat etm1 band 3, 4, 5 indicate satisfying separation between different classes, while the raw radar data had a high relative standard deviation $\frac{\delta}{\mu}$. The speckle noise in radar image leads to the variance of signal intensity. Especially the LDB and HDB classes have considerable high relative standard deviation, which is consistent with the misclassification in these two classes using unprocessed radar data. The entropy-filtered radar data significantly decreases the relative standard deviation, which indicates a better separation between land classes. For instance, the relative standard deviation of LDB and HDB decreased from 0.8 to 0.08, and 0.87 to 0.04, respectively. We found the entropy-processed Radarsat image has greater class separation than the raw Radarsat image, which explains some of the classification improvement.

We investigated merging several Radarsat feature combinations simultaneously with the Landsat images. We found

TABLE 3. CLASSIFICATION ACCURACIES FROM DIFFERENT SENSORS AND SENSOR COMBINATIONS

| Data Sets | Classification Accuracies | | | | | | | |
|------------|---------------------------|-----------|----------|---------|---------|---------|---------------|---------|
| | Forest (%) | Water (%) | Open (%) | LDB (%) | MDB (%) | HDB (%) | Transport (%) | All (%) |
| L1 | 83.91 | 90.07 | 40.96 | 66.77 | 59.33 | 56.96 | 70.64 | 66.89 |
| L1, Rr | 81.41 | 90.92 | 57.57 | 63.25 | 61.62 | 46.10 | 80.26 | 68.99 |
| L1, Re | 81.93 | 91.38 | 48.82 | 72.60 | 71.94 | 71.28 | 75.20 | 73.19 |
| L2 | 74.50 | 91.61 | 65.29 | 69.61 | 50.76 | 61.31 | 53.34 | 66.80 |
| L2, Rr | 74.14 | 90.45 | 71.40 | 68.56 | 53.82 | 54.43 | 58.89 | 67.57 |
| L2, Re | 76.12 | 92.84 | 70.44 | 76.65 | 70.34 | 72.07 | 57.59 | 73.86 |
| L1, L2 | 79.94 | 87.45 | 76.84 | 73.35 | 61.70 | 64.72 | 76.67 | 74.44 |
| L1, L2, Rr | 79.57 | 89.76 | 80.51 | 73.35 | 63.07 | 61.55 | 83.20 | 75.89 |
| L1, L2, Re | 81.48 | 92.61 | 84.12 | 79.64 | 73.78 | 74.92 | 80.42 | 81.04 |

*L1: Landsat February 2002; L2: Landsat June 2002; Rr: Raw Radarsat November 2001; Re: Radarsat November 2001 with entropy 13×13 window.

TABLE 4. SPECTRAL SIGNATURES OF SENSOR DATA SETS

| Land Type | L1 | | | | | | L2 | | | | | | R | | | |
|----------------|-------|----------|-------|----------|-------|----------|-------|----------|-------|----------|-------|----------|-------|----------|-------|----------|
| | B3 | | B4 | | B5 | | B3 | | B4 | | B5 | | r | | e | |
| | μ | σ |
| Forest | 44.4 | 9.8 | 50.9 | 11.9 | 67.9 | 18.2 | 44.4 | 19.1 | 111.2 | 13.5 | 83.5 | 18.7 | 57.9 | 38.1 | 2.1 | 0.2 |
| Water | 42.9 | 6.5 | 21.4 | 8.3 | 14.6 | 12.5 | 79.0 | 14.8 | 33.8 | 13.8 | 27.2 | 16.1 | 7.1 | 21.8 | 2.3 | 0.4 |
| Open | 55.5 | 10.8 | 62.5 | 21.4 | 76.7 | 17.1 | 97.1 | 35.5 | 83.6 | 21.7 | 146.3 | 47.9 | 31.1 | 23.0 | 2.1 | 0.3 |
| LDB | 59.0 | 10.4 | 72.5 | 10.5 | 70.6 | 11.0 | 76.3 | 19.5 | 95.2 | 8.0 | 103.6 | 15.4 | 51.7 | 41.4 | 2.4 | 0.2 |
| MDB | 51.8 | 8.8 | 53.8 | 10.0 | 58.4 | 10.9 | 68.9 | 17.5 | 84.0 | 12.7 | 90.0 | 15.0 | 55.5 | 37.0 | 2.1 | 0.1 |
| HDB | 64.8 | 17.1 | 51.9 | 13.5 | 62.5 | 19.7 | 118.3 | 38.3 | 70.4 | 17.5 | 120.7 | 42.3 | 72.6 | 62.9 | 2.5 | 0.1 |
| Transportation | 82.9 | 16.9 | 70.8 | 12.3 | 86.6 | 16.6 | 122.2 | 42.1 | 83.4 | 12.8 | 130.6 | 27.7 | 22.7 | 36.9 | 2.5 | 0.2 |

*L1: Landsat February 2002; L2: Landsat June 2002; R: Radarsat November 2001; μ : mean; σ : standard deviation; r: raw data; e: entropy 13×13 window.

the three processing techniques having the highest overall accuracy (i.e., an entropy 13×13 window, data range 9×9 window, and mean 19×19 window) increased the overall classification accuracy by about 10 percent compared to Landsat images alone. Both entropy and data range are texture measures of variability within the filtering window, and mean is the average value. Table 5 presents the classification accuracies from the fusion of Landsat data and these radar feature combinations. The radar feature combinations further improve the overall classification, as well as individual classes. Data range 9×9 and mean 19×19 together perform poorer than entropy 13×13 feature. Data range 9×9 and entropy 13×13 combinations increases overall accuracy by 2.03 percent than entropy 13×13 feature. Mean 19×19 and entropy 13×13 feature increase overall accuracy by 3.15 percent than entropy 13×13 feature. Overall accuracy from mean 19×19 and entropy 13×13 combination is about the same as the combination of mean 19×19 , entropy 13×13 and data range 9×9 . The fusion of the Landsat images and all three radar features generates the highest overall accuracy (84.36 percent), which is an increase of 9.92 percent from Landsat alone (74.44 percent). The classification accuracies increase more than 10 percent for the individual classes except forest and water (i.e., forest and water accuracies were high with only Landsat classification). Especially for HDB, the validation accuracy rises by 20.25 percent, from 64.72 percent to 84.97 percent.

Table 6 also provides the confusion matrix for the classification results of two Landsat data sets fused with these three Radarsat feature combinations. All individual classes demonstrate good consumer accuracy and producer accuracy (>70 percent). Rural classes (forest, water, and open) generally have higher accuracy than urban ones (LDB,

MDB, and HDB). Water achieves both highest consumer accuracy (98.18 percent) and producer accuracy (91.53 percent). LDB has the lowest consumer accuracy (78.57 percent), while MDB has the lowest producer accuracy (72.25 percent). The largest confusion occurs between LDB and MDB, although sensor fusion has improved the individual accuracy already. HDB and transportation also have relatively high misclassification.

Conclusion

In this study, we found significant accuracy improvement by using processed Radarsat data and Landsat data for mapping the land-cover types of the greater St. Louis area, when compared to Landsat data alone. For the St. Louis study area, the entropy processing consistently produces the larger improvements when compared to the other seven techniques. The fusion of Landsat data and Radarsat feature combinations from 13×13 entropy window, 9×9 data range widow and 19×19 mean filter window increased the overall accuracy by about 10 percent. This increase is a significant reduction in error of the overall land classification by about 38 percent (i.e., approximately an error of 26 percent reduced to an error of 16 percent).

Acknowledgments

This research is sponsored through a subcontract from Raytheon/STX Corporation. The authors would thank the Alaska Satellite Facility (ASF) for providing the Canadian Space Agency (CSA) Radarsat raw data. The cooperation of NASA for providing Landsat-7 ETM+ data is also greatly appreciated.

TABLE 5. CLASSIFICATION ACCURACIES FROM LANDSAT DATA AND RADARSAT FEATURE COMBINATIONS

| Data Sets | Classification Accuracies | | | | | | | |
|--------------------|---------------------------|-----------|----------|---------|---------|---------|---------------|---------|
| | Forest (%) | Water (%) | Open (%) | LDB (%) | MDB (%) | HDB (%) | Transport (%) | All (%) |
| L1, L2 | 79.94 | 87.45 | 76.84 | 73.35 | 61.70 | 64.72 | 76.67 | 74.44 |
| L1, L2, Rd | 81.70 | 88.53 | 84.04 | 75.82 | 63.99 | 73.34 | 80.51 | 78.32 |
| L1, L2, Rm | 83.17 | 89.61 | 80.22 | 82.34 | 57.65 | 73.02 | 87.03 | 78.99 |
| L1, L2, Re | 81.48 | 92.61 | 84.12 | 79.64 | 73.78 | 74.92 | 80.42 | 81.04 |
| L1, L2, Rd, Rm | 83.84 | 89.84 | 83.38 | 82.86 | 58.64 | 75.79 | 86.38 | 80.11 |
| L1, L2, Rd, Re | 82.29 | 91.22 | 86.40 | 80.69 | 74.31 | 80.70 | 85.97 | 83.07 |
| L1, L2, Rm, Re | 82.66 | 92.69 | 85.88 | 84.13 | 71.10 | 85.60 | 87.60 | 84.19 |
| L1, L2, Rd, Rm, Re | 83.61 | 91.53 | 87.57 | 83.68 | 72.25 | 84.97 | 87.03 | 84.36 |

*L1: Landsat February 2002; L2: Landsat June 2002; Rd: Radarsat November 2001 with data range 9×9 window; Rm: Radarsat November 2001 with mean 19×19 window; Re: Radarsat November 2001 with entropy 13×13 window.

TABLE 6. CONFUSION MATRIX FOR CLASSIFICATION VALIDATION OF LANDSAT FEBRUARY 2002, JUNE 2002, AND RADARSAT FEATURE COMBINATIONS

| | Forest (Pixel) | Water (Pixel) | Open (Pixel) | LDB (Pixel) | MDB (Pixel) | HDB (Pixel) | Transport (Pixel) | CA (%) | EC (%) |
|-----------|-------------------|------------------|-----------------|----------------|----------------|----------------|----------------------|-----------|-----------|
| Forest | 1138 | 9 | 22 | 52 | 127 | 7 | 0 | 83.99 | 16.01 |
| Water | 0 | 1189 | 16 | 0 | 1 | 0 | 5 | 98.18 | 1.82 |
| Open | 68 | 24 | 1191 | 26 | 42 | 21 | 20 | 85.56 | 14.44 |
| LDB | 64 | 3 | 20 | 1118 | 133 | 52 | 33 | 78.57 | 21.43 |
| MDB | 89 | 0 | 13 | 114 | 945 | 20 | 6 | 79.61 | 20.39 |
| HDB | 2 | 58 | 57 | 19 | 57 | 1074 | 95 | 78.85 | 21.15 |
| Transport | 0 | 16 | 41 | 7 | 3 | 90 | 1067 | 87.17 | 12.83 |
| PA (%) | 83.61 | 91.53 | 87.57 | 83.68 | 72.25 | 84.97 | 87.03 | | |
| EO (%) | 16.39 | 8.47 | 12.43 | 16.32 | 27.75 | 15.03 | 12.97 | | |

*CA: consumer accuracy; PA: producer accuracy; EO: errors of omission; EC: errors of commission.

References

- Benediktsson, J.A., and I. Kanellopoulos, 1999. Classification of multisource and hyperspectral data based on decision fusion, *IEEE Transactions on Geosciences and Remote Sensing*, 37(3): 1367–1377.
- Campbell, J.B., 1996. *Introduction to Remote Sensing*, Guilford Press, New York, pp. 366–370.
- Curlander, J.C., and R.N. McDonough, 1991. *Synthetic Aperture Radar System and Signal Processing*, John Wiley and Sons Press, New York, pp. 671–672.
- Dobson, M.C., F.T. Ulaby, T.L. Toan, A. Beadoin, E.S. Kasischke, and N. Christensen, 1992. Dependence of radar backscatter on coniferous forest biomass, *IEEE Transactions on Geosciences and Remote Sensing*, 30(2):412–415.
- Donnay, J., M.J. Barnsley, and P.A. Longley, 2001. *Remote Sensing and Urban Analysis*, Taylor and Francis, New York, pp. 3–11.
- Goetz, S.J., S.D. Prince, M.M. Thawley, A.J. Smith, R. Wright, and M. Weiner, 2000. Applications of multi-temporal land cover information in the mid-Atlantic region: A RESAC initiative, *Proceedings of the International Geoscience and Remote Sensing Symposium*, 24–28 July, Honolulu, Hawaii, 1:357–359.
- Gong, P., and P.J. Howarth, 1990. The use of structural information for improving land-cover classification accuracies at the rural-urban fringe, *Photogrammetric Engineering & Remote Sensing*, 56(1):67–73.
- Gonzalez, R.C., 1987. *Digital Image Processing*, Addison-Wesley Publishing Company, Reading, Massachusetts, p. 503.
- Green, K., D. Kempka, and L. Lackey, 1994. Using remote sensing to detect and monitor land-cover and land-use change, *Photogrammetric Engineering & Remote Sensing*, 60(3):331–337.
- Haack, B.N., and E.T. Slonecker, 1994. Merged spaceborne radar and thematic mapper digital data for locating villages in Sudan, *Photogrammetric Engineering & Remote Sensing*, 60(10): 1253–1257.
- Haack, B.N., N.D. Herold, and M.A. Bechdol, 2000. Radar and optical data integration for land-use/land-cover mapping, *Photogrammetric Engineering & Remote Sensing*, 66(6): 709–716.
- Hagg, W., and M. Sties, 1994. Efficient speckle filtering of SAR images, *Proceedings of the International Geoscience and Remote Sensing Symposium*, 08–12 August, Pasadena, California, 4:2140–2142.
- Haralick, R.M., 1973. Textural Features in Image Classification, *IEEE Transactions on Systems, Man and Cybernetics*, 3:610–621.
- Ji, C.Y., 2000. Land-use classification of remotely sensed data using Kohonen self-organizing feature map neural networks, *Photogrammetric Engineering & Remote Sensing*, 66(12):1451–1460.
- Kurosu, T., S. Uratsuka, H. Maeno, and T. Kozu, 1999. Texture statistics for classification of land use with multitemporal JERS-1 SAR single-look imagery, *IEEE Transactions on Geosciences and Remote Sensing*, 37(1):227–235.
- Ludeman, L.C., 1986. *Fundamental of Digital Signal Processing*, Harper and Row, New York, New York, 330 p.
- Paola, J.D., and R.A. Schowengerdt, 1995. A detailed comparison of backpropagation neural network and maximum-likelihood classifiers for urban land use classification, *IEEE Transactions on Geosciences and Remote Sensing*, 30(4):981–996.
- Proakis, J.G., and J.G. Manolakis, 1996. *Digital Signal Processing Principles, Algorithm and Applications*, Prentice Hall, Upper Saddle River, New Jersey, 968 p.
- Richards, J.A., 1990. Radar backscatter modeling of forests: A review of current trends, *International Journal of Remote Sensing*, 11(7):1299–1312.
- Russ, J.C., 1992. *The Image Processing Handbook*, CRC Press, Boca Raton, Florida, p. 445.
- Singh, A., 1989. Digital change detection techniques using remotely-sensed data, *International Journal of Remote Sensing*, 10(6): 989–1003.
- Solberg, A.H.S., and K.J. Anil, 1997. Texture fusion and feature selection applied to SAR imagery, *IEEE Transactions on Geosciences and Remote Sensing*, 35(2):475–479.
- Strozzi, T., P.B.G. Dammert, U. Wegmuller, J.M. Martinez, and J.I.H. Askne, 2000. Land use mapping with ERS SAR interferometry, *IEEE Transactions on Geosciences and Remote Sensing*, 38(2):766–775.
- Tapley, B.D., M.M. Crawford, T. Howard, K.D. Hutchison, S. Smith, and G.L. Wells, 2001. Application of EOS Core System data and data products for monitoring and mitigating natural disasters, *Proceedings of the International Geoscience and Remote Sensing Symposium*, 09–13 July, 18 Sydney, Australia, 2:824–826.
- Ulaby, F.T., R.K. Moore, and A.K. Fung, 1982. *Microwave Remote Sensing Active and Passive From Theory to Applications, Vol. III*, Artech House, Massachusetts, pp. 1115–1120.
- Won, J.S., H.Y. Kim, and J.H. Ryu, 1999. Coastal geomorphologic change detection using SAR and optical remote sensing data at the Nakdong river estuary, Korea, *Proceedings of the International Geoscience and Remote Sensing Symposium*, 28 June–02 July, Hamburg, Germany, 6:2733–2735.

(Received 05 July 2005; accepted 19 August 2005; revised 10 October 2005)